*Journal of Applied Fluid Mechanics*, Vol. 19, No. 1, pp. 3221-3235, 2026. Available online at <a href="https://www.jafmonline.net">www.jafmonline.net</a>, ISSN 1735-3572, EISSN 1735-3645. <a href="https://doi.org/10.47176/jafm.19.1.3715">https://doi.org/10.47176/jafm.19.1.3715</a>



## Effects of Electrical Boundary Configurations on Magnetohydrodynamic Flow and Heat Transfer in a Liquid Metal-filled Annulus

B. Mahfoud <sup>1†</sup>, L. Bouragbi <sup>2</sup> and H. E. Mahfoud <sup>3</sup>

<sup>1</sup> Mechanics and Energy Laboratory (LME), Faculty of Applied Science- University of Bouira, 10000, Algeria Department of Process Engineering, Faculty of Technology-University 20 août 1955–Skikda, 21000, Algeria

<sup>3</sup> Department of Computer sciences, Faculty of Technology -University 20 août 1955–Skikda, 21000, Algeria

† Email: <u>b.mahfoud@univ-bouira.dz</u>

#### ABSTRACT

This numerical study investigates magnetohydrodynamic (MHD) flow and heat transfer for liquid metals within a cylindrical annulus subjected to a radial magnetic field. A parametric study compares the thermal behavior of these metals under identical conditions, with particular focus on the influence of the annular wall's electrical boundary conditions on heat transfer. The finite volume method is used to analyze three electrical boundary conditions: electrically insulated walls (EI), electrically conducting vertical walls (EC-V), and electrically conducting horizontal walls (EC-H). The findings show that magnetic field strength, annular gap, aspect ratio, and wall conductivity significantly affect temperature distribution, average Nusselt number, Lorentz force, and induced electric field. The Nusselt number increases when the aspect ratio is below unity but decreases when it is above unity, and it improves consistently with a larger annular gap. Stronger magnetic fields are required to sustain conduction-dominated regimes in thicker annuli. The magnetic field generates characteristic Hartmann and Roberts layers through Lorentz force interactions, with layer dissipation observed in conducting wall cases. Among the configurations, the EC-H case exhibits the highest heat transfer performance compared to EI boundaries, particularly for intermediate gap ratios (R  $\approx$  0.5–0.87). (EC-H) offers the best heat transfer overall, with up to 10% gains for R<0.87, while (EI) performs better for R>0.87, and (EC-V) remains the least efficient.

#### Article History

Received June 5, 2025 Revised September 3, 2025 Accepted September 5, 2025 Available online November 5, 2025

#### Keywords:

Annulus Electrical boundary Hartmann layer Liquid metal Magnetic field Roberts layer

#### 1. Introduction

The efficient management of heat in industrial systems is critical to the performance, safety, and sustainability of energy and manufacturing technologies. Amongst the various heat transfer media, liquid metals such as potassium (K), lithium (Li), and sodiumpotassium (NaK) have garnered significant attention due to their exceptional thermal properties and unique applicability across a broad temperature spectrum (Wang et al., 2021). Each of these metals exhibits distinct advantages and limitations which influence their integration into specialised cooling and heat exchange systems. Liquid K, with its low melting point and high thermal conductivity, is particularly suited for moderatetemperature applications such as NaK eutectic cooling in fast-breeder nuclear reactors (Abou-Sena et al., 2016). In contrast, Li, characterised by its high specific heat and role in tritium breeding, is increasingly vital for highperformance systems like fusion reactors and aerospace thermal regulation (Roux et al., 1992). Molten NaK, though less commonly used as a fluid medium, offers exceptional thermal stability at ultra-high temperatures, making it indispensable in extreme environments such as metallurgical processing and space-based power systems (Ulyanov et al., 2024). Understanding the comparative thermophysical behaviour, reactivity, and compatibility of these metals with containment materials is essential for optimising heat transfer processes.

However, the interaction between liquid metals and external forces, particularly magnetic fields, introduces another layer of complexity and opportunity. Magnetic fields have emerged as a transformative tool for controlling heat transfer in systems involving electrically conductive fluids, such as liquid metals (Ni et al., 2025). For instance, in fusion reactors (e.g. ITER), liquid lithium is exposed to intense magnetic fields to confine

Nome	NOMENCLATURE						
A	aspect ratio	Ra	Rayleigh number				
В	magnitude of the external magnetic field (Tesla)	T	temperature				
<i>E</i> '	dimensional induced electric field	<i>u, v, w</i>	dimensionless radial, axial, azimuthal velocity components				
E	dimensionless induced electric field						
$f_L$	Lorentz force	Greek s	ek symbols				
$F_L$	dimensionless Lorentz force	$\alpha$	thermal diffusivity of the fluid				
g	acceleration due to gravity	$oldsymbol{eta}$	thermal expansion coefficient				
H	height of cylindrical annulus	$\Theta$	dimensionless temperature				
На	Hartmann number	$\nu$	kinematic viscosity of the fluid				
j	electric current density	λ	thermal conductivity				
J	dimensionless electric current density	$\rho$	density of the fluid				
$k_w$	conductance ratio	$\sigma$	electric conductivity				
Nu	local Nusselt number	Φ	dimensionless electric potential				
P	dimensionless pressure	Subscrip	Subscripts				
Pr	Prandtl number	c	cold condition at wall				
R	annular gap	h	hot condition at wall				
r, θ, z	dimensionless spatial coordinates	w	wall				

plasma and optimise heat extraction via magnetohydrodynamic (MHD) effects (Yan, 2024). Similarly, NaK alloys can be magnetically manipulated to stabilise turbulent flows or induce forced convection currents, enhancing thermal transfer efficiency (Leonchuk et al., 2022).

These principles extend to advanced reactor designs like Tokamaks. In such systems, natural convection in liquid metal blankets (e.g. HCLL, DCLL, HPCB) avoids the high pressure drops inherent in forced flow under strong magnetic fields whilst simultaneously enabling tritium breeding (Boccaccini, 2013). Magnetic fields counteract the instabilities inherent in natural convection systems, such as chaotic flow patterns caused by temperature gradients. By generating Lorentz forces which suppress fluid movement, they improve system performance, material uniformity, and safety (Kumar & Singh, 2013; Mozayyeni & Rahimi, 2012). This stabilisation is critical in applications such as crystal growth or metallic melt processing, where flow symmetry and thermal uniformity are paramount (Kakarantzas et al., 2014; Teimouri et al., 2015). Studies (Sankar et al., 2011) have demonstrated that magnetic field orientation (axial, radial, or transverse) plays a decisive role in modulating flow dynamics between coaxial cylinders. For example, transverse magnetic fields are more effective than axial ones in influencing the Nusselt number and thermal performance (Afrand, 2017), whereas the Hartmann number's impact on heat transfer can outweigh that of the Rayleigh number by a factor of 4 (Wrobel et al., 2010). The interaction between the annular geometry and fluid velocity plays a critical role in vortex formation and recirculation zones, whilst magnetic fields significantly influence flow stability (Ali et al., 2023; Benhacine et al., 2022a; Mahfoud, 2022).

These interactions stabilise swirling flows, reduce oscillations in thermocapillary convection, and suppress vortex formation, as shown in studies of cylindrical and annular containers (Dash & Singh, 2019; Wang et al., 2015). The intersection of nanotechnology and MHD has

further expanded these applications. Magnetic nanofluids and thermally efficient nanoparticles enhance heat transfer, stabilise flows, and improve energy efficiency, as demonstrated in studies by Benhacine et al. (2022b), Selim et al. (2023) and Mahfoud (2023).

The induced magnetic field is critically important in MHD, particularly under high magnetic Reynolds number conditions, with applications in MHD power generation, geophysics, oil purification, and glass manufacturing. Experimental studies by Jha and Aina (2018) have established that field intensity escalates with the magnetic interaction parameter (M) and magnetic Prandtl number (Pm) in microchannels, significantly modifying velocity profiles and amplifying skin friction in annular geometries. Conversely, Leela et al. (2022) have observed diminished field strength with elevated M and Pm when viscous and ohmic dissipation are considered. Sankar et al. (2006) numerically confirmed that increased radii ratios reduce the Hartmann number whilst enhancing the Nusselt number, noting superior performance of radial magnetic fields in large cavities. Computational approaches predominantly employ the Finite Element Method (FEM) and the Finite Difference Method (FDM), though the Meshless Finite Difference Method (MFDM) offers greater flexibility and efficiency lower accuracy. To address simulation despite complexity, artificial intelligence (AI) techniques, including ANNs (Shoaib et al., 2021), are increasingly utilised, revealing velocity suppression by M and enhancement second-grade fluid/Marangoni by parameters. Complementary work by Shilpa et al. (2023) on annular convection has demonstrated that Lorentz forces reduce velocity and field strength at higher values of Pm and M, whilst mixed convection parameters intensify the induced magnetic field.

Building on this foundation, our study advances prior research by addressing two critical yet overlooked aspects of MHD convection: wall electrical conductivity and induced electric potential. Unlike analyses assuming insulating boundaries, we systematically examine MHD convection in a vertical annular channel filled with an electrically conducting fluid under a radial magnetic field. Key parameters: magnetic field strength, annular gap dimensions, aspect ratio, and wall conductivity are analyzed for their coupled effects on heat transfer (Nusselt number), flow structure, Lorentz forces, and induced electric fields. These insights aim to refine liquid-metal cooling systems in applications demanding precise thermal management and operational safety, such as advanced nuclear reactors.

# 2. FORMULATION OF THE MATHEMATICAL MODEL

#### 2.1 Model

This investigation focuses on steady-state, threedimensional laminar natural convection of liquid metals within a vertical cylindrical annulus subjected to a uniform radial magnetic field. The geometric configuration comprises two concentric cylinders with inner radius  $r_{inner}$ , outer radius  $r_{outer}$ , and height H, defining an annular gap characterized by the dimensionless parameter  $R = (r_{outer} - r_{inner})/r_{outer}$ . A radial magnetic field  $\mathbf{B}=B\mathbf{e}_r$  is imposed, generating distinct boundary layers and accounting for induced magnetic effects. The inner cylinder is maintained at a high temperature  $T_h$ , while the outer cylinder is cooled to  $T_c$  $(T_c < T_h)$ , establishing a radial temperature gradient that drives buoyancy-driven flow. Three electrical boundary configurations are explored: fully insulated walls (EI), conductive vertical inner/outer cylindrical walls (EC-V), and conductive horizontal top/bottom surfaces (EC-H) to evaluate their impact on magnetohydrodynamic (MHD) interactions and thermal transport. Aspect ratios  $(A=H/r_{outer})$  spanning 0.5–3 and annular gaps (R) of 0.5– 0.9 are analyzed to quantify their influence on flow patterns and heat transfer.

The fluid is treated as incompressible and Newtonian, with constant thermophysical properties except for density variations in the buoyancy term (Boussinesq approximation). Rigid no-slip conditions are enforced at all walls. Joule heating, viscous dissipation, thermal radiation, and Hall effects are neglected to isolate primary MHD-convective coupling. The employed approximations are validated for the present configuration, where operating temperatures remain below 100°C and the Hartmann number (Ha) is constrained to Ha < 100. These thresholds align with established regimes where viscous forces dominate electromagnetic effects, ensuring model fidelity as documented in prior MHD studies (Afrand, 2017, Wrobel et al., 2010). The governing equations, mass conservation, momentum (including Lorentz forces), energy transport, and electric potential are formulated in cylindrical coordinates to resolve coupled thermal and electromagnetic phenomena. Figure 1 depicts the system geometry and boundary conditions.

### 2.2. Mathematical Formulation

Mass Conservation:

The incompressibility condition is expressed as:

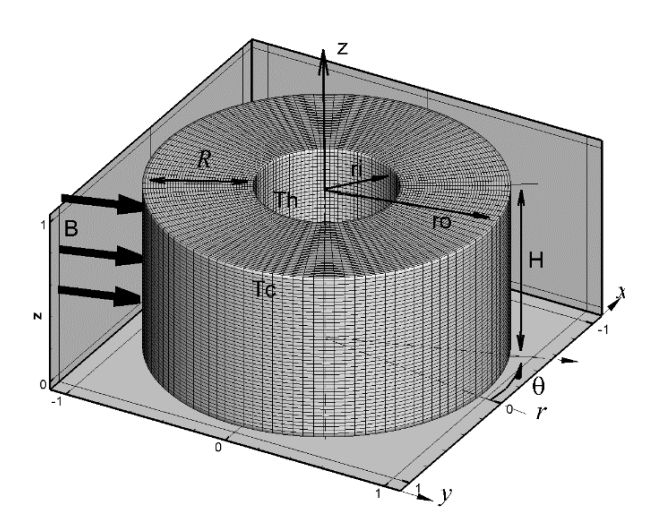


Fig. 1 Schematic and structured grid of the present model

$$\nabla \cdot \boldsymbol{U} = 0 \tag{1}$$

where  $\boldsymbol{U}$  is the vector of velocity.

- The momentum equation:

$$\rho\left(\frac{\partial \boldsymbol{U}}{\partial t} + (\boldsymbol{\nabla}.\boldsymbol{U})\boldsymbol{U}\right) = -\boldsymbol{\nabla}p + \rho\nu[\boldsymbol{\nabla}^2\boldsymbol{U}] + Forces \qquad (2)$$

and in presence of buoyancy force and magnetic field, we have: Forces =  $\rho g + (j \times B)$ .

Here, P,  $\rho$  and v are respectively pressure, density and kinematic viscosity. The Lorentz force  $f_L = j \times B$  arises from the interaction between the current density j and magnetic field B.

#### - Energy Equation:

Neglecting viscous and ohmic dissipation, the temperature field *T* is governed by:

$$(\mathbf{U}.\mathbf{\nabla})T = \alpha[\mathbf{\nabla}^2 \mathbf{T}] \tag{3}$$

where  $\alpha$  is the thermal diffusivity.

- Electric potential (Afrand, 2017)

$$\nabla^{2} \varphi = \nabla \cdot (\mathbf{U} \times \mathbf{B}) = \underbrace{\mathbf{U} \cdot (\nabla \times \mathbf{B})}_{0} + \mathbf{B} \cdot (\nabla \times \mathbf{U})$$
 (4)

In which B is the vector of magnetic field. Since the constant magnetic field is considered in this study, the term of U. ( $\nabla \times B$ ) becomes zero.

The current density J and induced electric field E are related by:

$$\mathbf{j} = \sigma[\mathbf{E}' + \mathbf{U} \times \mathbf{B}], \ \mathbf{E}' = -\nabla \varphi \tag{5}$$

**Table 1 Nondimensionalization Parameters** 

Dim	Nondim	Dim	Nondim
Form	Form	Form	Form
u′	$u = (u' \cdot R)/\alpha$	p	$P = (p \cdot R^2)/(\rho \cdot \alpha^2)$
v'	$v = (v' \cdot R)/\alpha$	T	$\Theta = (T - T_c)/(T_h - T_c)$
w'	$w = (w' \cdot R)/\alpha$	φ	$\Phi = \varphi / (\alpha \cdot B)$
r'	r = r' / R	E'	$E = (E' \cdot R)/(\alpha \cdot B)$
z'	z = z' / R	$f_L$	$F_L = (f_L \cdot R)/(\alpha \cdot \sigma \cdot B^2)$

where  $\sigma$  is electrical conductivity.

Non-dimensionalization is achieved via scaling parameters:

Substituting into in Eqs. (1)-(5) yields:

- Continuity:

$$\frac{\partial \mathbf{u}}{\partial r} + \frac{1}{r} \frac{\partial v}{\partial \theta} + \frac{\partial w}{\partial z} = 0 \tag{6}$$

- Radial momentum:

- Axial momentum:

$$\left(u\frac{\partial v}{\partial r} + \frac{w}{r}\frac{\partial v}{\partial \theta} + v\frac{\partial v}{\partial z}\right) = -\frac{\partial P}{\partial r} + Pr(\nabla^2 v) + Ha^2.F_{Lz}$$
(8)

- Azimuthal momentum:

$$\begin{split} u\frac{\partial w}{\partial r} + \frac{w}{r}\frac{\partial v}{\partial \theta} + v\frac{\partial w}{\partial z} + \frac{uw}{r} &= -\frac{1}{r}\frac{\partial P}{\partial \theta} + \\ Pr\left(\nabla^2 w - \frac{w}{r^2} + \frac{2}{r^2}\frac{\partial u}{\partial \theta}\right) + +Ha^2.F_{L\theta} \end{split} \tag{9}$$

 $F_{Lz}=(-\frac{1}{r}\frac{\partial\Phi}{\partial\theta}+v); \ F_{L\theta}=(\frac{\partial\Phi}{\partial z}+w)$  are the axial and azimuthal component of the Lorentz force.  $(F_{Lr}=0)$  because  $j\times B=0$  has no radial component when  $B=Be_r$ 

Energy conservation:

$$u\frac{\partial\Theta}{\partial r} + \frac{w}{r}\frac{\partial\Theta}{\partial\theta} + v\frac{\partial\Theta}{\partial z} = \nabla^2\Theta$$
 (10)

- Electric potential:

$$\frac{1}{r}\frac{\partial}{\partial r}\left(r\frac{\partial\Phi}{\partial r}\right) + \frac{1}{r^2}\frac{\partial^2\Phi}{\partial \theta^2} + \frac{\partial^2\Phi}{\partial z^2} = \frac{\partial v}{\partial \theta} - \frac{\partial w}{\partial z} \tag{11}$$

Key dimensionless groups include:

Prandtl number:  $Pr=v/\alpha$  (momentum vs. thermal diffusivity).

Rayleigh number:  $Ra = \beta g \Delta T R^3 / \nu \alpha$  (buoyancy vs. viscous forces)

Hartmann number:  $Ha = BR\sqrt{\frac{\sigma}{\rho\nu}}$  (Lorentz vs. viscous forces).

Heat Transfer Quantification: Local and average Nusselt numbers (*Nu*) quantify convective efficiency along inner/outer walls (Kakarantzas et al., 2014):

$$Nu(\theta) = -\ln(\frac{r_i}{r_o}) \left( r \frac{\partial \theta}{\partial r} \right) \Big|_{r=r_{inner}; \ r_{outer}}$$
 (13)

The azimuthally-averaged Nusselt numbers (Kakarantzas et al., 2014):

$$Av - Nu = \left(\frac{1}{2\pi}\right) \int_0^{2\pi} Nu(\theta) d\theta \tag{14}$$

While the overall (i.e., axially and azimuthally averaged) Nusselt numbers at the inner and outer walls are calculated as follows:

$$Av - Nu = \left(\frac{1}{H\pi}\right) \int_0^{2\pi} \int_0^H Nu(\theta) dz d\theta \tag{15}$$

- Boundary Conditions:

The system's boundaries are defined by hydrodynamic, thermal, and electromagnetic constraints as follows:

All Walls: No-slip condition (U=0) is enforced at all solid surfaces. Summary of the boundary conditions employed in the study (Table 2).

Table 2 Boundary conditions

Boundary	Thermal	Electromagnetic
Inner wall $(r = r_{inner})$	$\Theta = 1$ (hot wall)	Conductive
		$\sigma \frac{\partial \Phi}{\partial \mathbf{r}} = \sigma_w \frac{\partial \Phi_w}{\partial \mathbf{r}}$
		Insulated: $\frac{\partial \Phi}{\partial r} = 0$
Outer wall $(r = r_{outer})$	$\Theta = 0$ (cold wall)	Conductive
		$\sigma \frac{\partial \Phi}{\partial \mathbf{r}} = \sigma_w \frac{\partial \Phi_w}{\partial \mathbf{r}}$
		Insulated: $\frac{\partial \Phi}{\partial r} = 0$
Top wall $(z = H)$	$\partial \Theta / \partial z = 0$ (thermally	$\partial \Phi / \partial z = 0$
Bottom wall $(z = 0)$	insulated)	(no vertical current)

For electrically conductive wall, continuity of the radial current at the fluid-wall interface is enforced:  $\sigma \frac{\partial \Phi}{\partial r} = \sigma_w \frac{\partial \Phi_w}{\partial r}; \quad \text{where } \sigma \text{ is the fluid's electrical conductivity, } \sigma_w \text{ is the wall conductivity, } \text{ and } \Phi_w \text{ is the wall potential.} The conductance ratio <math>k_w = \sigma_w \, e_w / \sigma \, R$  links wall properties (thickness  $e_w$ , conductivity  $\sigma_w$ ) to fluid and geometric parameters. When wall conductance dominates ( $k_w \gg 1$ ), the boundary condition simplifies to  $\Phi_w = \text{constant.}$  This ideal conductor approximation is physically justified as dominant wall conductance short-circuits radial currents, decoupling their behavior from the fluid.

# 3. NUMERICAL SOLUTION, GRID SIZES AND VALIDATION

#### 3.1 Numerical Solution

The governing equations are discretized using a finite-volume method (FVM) on a staggered cylindrical grid, ensuring robust prevention of pressure-velocity decoupling. To resolve critical magnetohydrodynamic (MHD) boundary layers, specifically the Hartmann layers (thickness scaling as  $\sim 1/Ha$ ) and Roberts  $\sim 1/\sqrt{Ha}$ ), a non-uniform layers (thickness refinement is applied near boundaries. For spatial discretization, second-order central differences are used for diffusion terms, while the third-order QUICK scheme minimizes numerical diffusion in advection terms. Temporal integration follows a pseudo-transient IMEX strategy: diffusion terms are treated implicitly via the Crank-Nicolson method, and nonlinear advection terms are integrated explicitly using a third-order Runge-Kutta (RK3) scheme. Mass conservation is rigorously enforced through the fractional-step method, with pressure correction computed via an FFT-accelerated Poisson solver (Boyd, 2000). The electric potential is solved iteratively using the GMRES algorithm with ILU preconditioning, and electromagnetic boundary conditions at conducting walls are robustly enforced through Nitsche's method (Ben Salah et al., 2001).

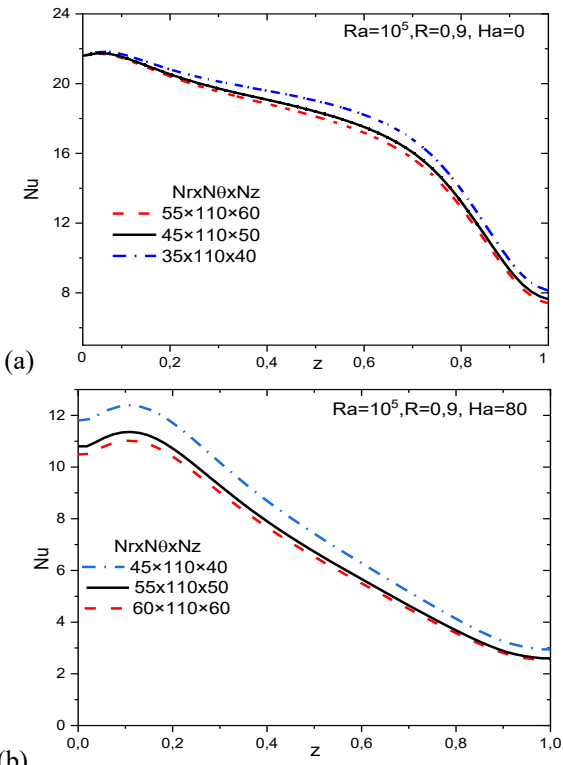


Fig. 2 Profiles of the local Nusselt number for different grid resolutions (A = 1, R = 0.9, Ra = 10<sup>5</sup>), with H = 0 (top) and Ha = 80 (bottom)

#### 3.2. Grid Independence

A comprehensive mesh sensitivity analysis was conducted for the most computationally demanding case (A=1,R=0.9) at Ha=0. Three mesh resolutions were compared: a coarse grid  $(35\times110\times40$  nodes), an intermediate grid  $(45\times110\times50)$ , and a finer grid  $(55\times110\times60)$ . Key validation metrics included the local Nusselt number (Nu) on the inner wall. Results demonstrated <3% deviation between the coarse and fine grids, validating the computational efficiency of the coarser mesh. To optimize accuracy, geometric stretching (5-10% growth) was applied near boundaries, while the azimuthal node count  $(N_\theta=110)$  was fixed to preserve three-dimensional flow effects.

For simulations involving a magnetic field (Ha > 0), additional radial grid refinement is applied to properly resolve the Hartmann and Roberts boundary layers. The final mesh configurations, selected based on the Hartmann number (Ha), are scalable: a mesh with 45 radial, 110 azimuthal and 50 axial cells (45R  $\times$  110  $\times$  50A) was used for Ha  $\leq$  5. For Ha  $\geq$  20, a finer mesh (65R×110×65A) was adopted, featuring increased radial and axial resolution to accurately capture the effects of Lorentz forces. A comparison grid for Ha=80 is shown in Fig. 2b.

#### 3.3 Validation

The numerical model was thoroughly validated against both experimental data and high-fidelity numerical benchmarks, confirming its accuracy under diverse thermal and geometric configurations. The first

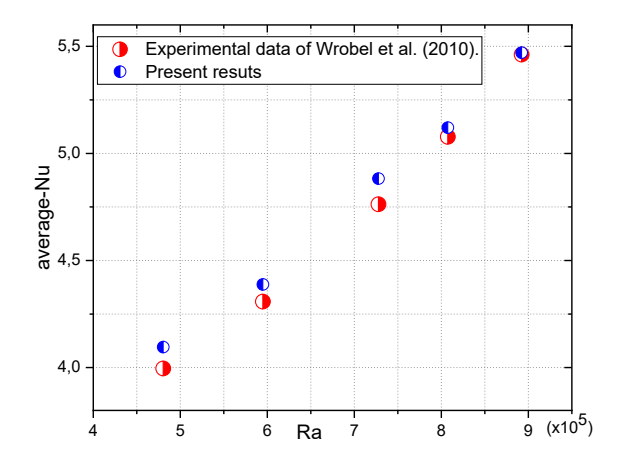


Fig. 3 Comparison of average Nusselt number results with experimental data of Wrobel et al. (2010)

validation utilized experimental results from Wrobel et al. (2010), which involved a high-Prandtl-number fluid (Pr = 61), a diameter ratio of 2.7, and an aspect ratio of 5.41. The model demonstrated excellent agreement, with deviations in the average Nusselt number remaining below 5%, as shown in Fig. 3.

A second validation compared our results against the DNS study of Kakarantzas et al. (2014), which analyzed magnetohydrodynamic (MHD) flow between vertically oriented coaxial cylinders under internal volumetric heating. Their configuration featured a Hartmann number (Ha = 100), radius ratio (R = 2Ri), Rayleigh number (Ra =  $10^4$ ), radially applied magnetics stabilization, thermally insulated end caps, and isothermal cylindrical walls (Fig. 4). Our model reproduced the flow structures and heat transfer behavior with a relative error of 5%, confirming its reliability for magnetic field-influenced natural convection simulations. Figure 5 further validates this agreement by comparing axial velocity profiles versus radius at  $\theta$ =0° and  $\theta$ =90°, evaluated at three vertical positions.

#### 4. RESULTS AND DISCUSSION

In magnetohydrodynamics, the behavior of the system is dictated by the interaction of an electrically conducting fluid (such as liquid) with an externally imposed magnetic field. As the fluid moves through the magnetic field, electric currents are induced within the fluid, giving rise to a Lorentz force that acts perpendicular to both the flow direction and the magnetic field lines. This force significantly modifies the fluid dynamics, resulting in complex distributions of velocity and current throughout the domain.

To establish appropriate simulation parameters, a preliminary comparison was conducted between Rayleigh numbers Ra=10<sup>4</sup> and Ra=10<sup>5</sup>. The results showed that the higher Rayleigh number (Ra=10<sup>5</sup>) leads to stronger convective effects, thereby offering better insight into coupled thermal and hydrodynamic interactions. Consequently, all subsequent simulations were performed at Ra=10<sup>5</sup>. A second parametric study

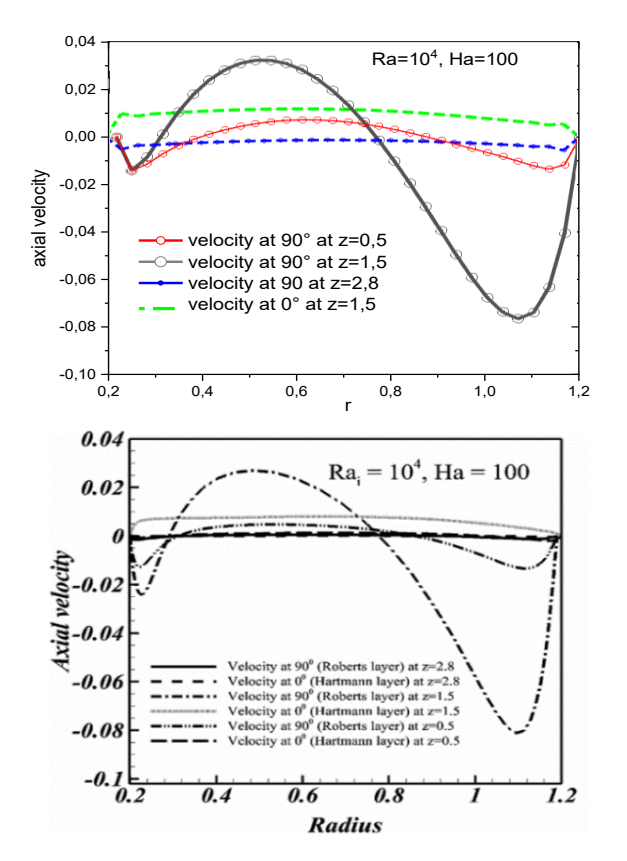


Fig. 4 Comparison of axial velocity, our result (top) with Kakarantzas et al. (2014) at bottom

examined the influence of different Prandtl numbers associated with various liquid metals: potassium (Pr=0.072), lithium (Pr=0.055), and a sodium-potassium eutectic alloy (Pr=0.037).

To assess the effect of boundary electrical properties on MHD behavior and heat transfer performance, three distinct electrical boundary conditions were investigated. In the first configuration Electrically Insulated Walls (EI), all boundaries, including the inner and outer cylindrical surfaces and the top and bottom horizontal walls, were assumed to be electrically insulating, thereby inhibiting any current exchange with the surroundings. second configuration Electrically Conductive Vertical Walls (EC-V) allowed electrical conduction through the vertical (cylindrical) walls, enabling radial current flow, while the horizontal boundaries remained insulated. In the third configuration Electrically Conductive Horizontal Walls (EC-H) only the top and bottom surfaces were electrically conductive, allowing vertical current penetration, whereas the cylindrical walls were kept insulated. These configurations provide a framework for understanding how wall conductivity influences current distribution, fluid motion, and thermal transport within the annular cavity.

To comprehensively characterize system behavior under varying geometrical and electromagnetic conditions, simulations were performed for a range of aspect ratios A=0.5, 1, 2, and 3, as well as dimensionless gap widths R=0.5, 0.6, 0.7, 0.8, 0.9. This systematic exploration enables detailed insights into the combined

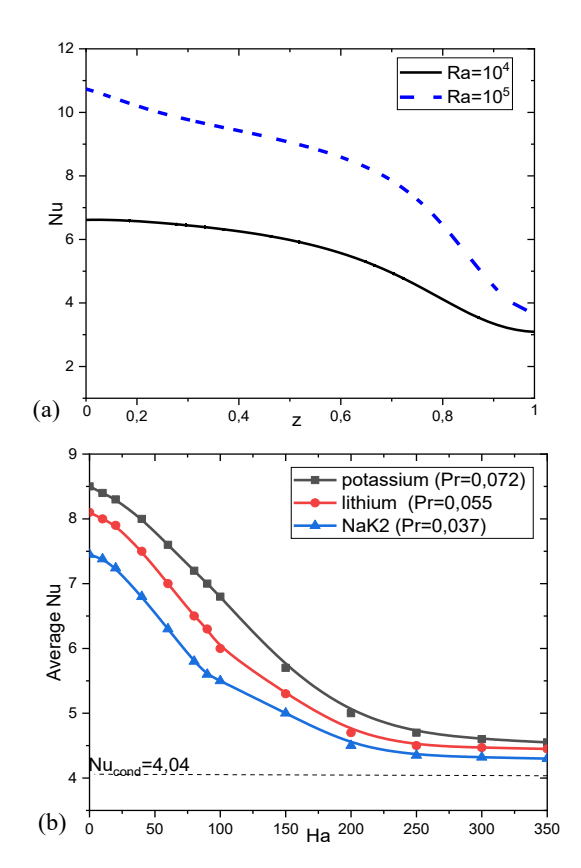


Fig. 5 Influence of (a) Rayleigh number Ra and (b) Prandtl and Hartmann numbers on the average Nusselt number

effects of geometry and boundary conditions on MHD flow and heat transfer performance.

### 4.1 Influence of Key Parameters on Heat Transfer

This section investigates the influence of five key dimensionless parameters, namely, the Prandtl number (Pr), Rayleigh number (Ra), Hartmann number (Ha), aspect ratio (A), and annular gap (R) on convective heat transfer in natural convection flows within annular geometries. The average Nusselt number (Nu) is used as the primary metric to quantify heat transfer performance. Among these parameters, the Hartmann number, representing the ratio of electromagnetic to viscous forces, plays a crucial role in modulating the flow structure and heat transport behavior.

An initial comparison between Ra = 10<sup>4</sup> and Ra = 10<sup>5</sup> shows that the latter generates much stronger convective currents, making it the more suitable choice for analyzing coupled thermal and hydrodynamic interactions. Therefore, all subsequent simulations are conducted at Ra = 10<sup>5</sup> (see Fig. 5a). A second analysis examines three Prandtl numbers (Pr = 0.072, 0.055, and0.037) corresponding to liquid potassium, lithium, and a sodium-potassium eutectic alloy, respectively. Figure 5b illustrates the combined effects of Prandtl and Hartmann numbers on the average Nusselt number in an annular configuration with a gap ratio R = 0.9. As shown, the average Nusselt number consistently increases with the Prandtl number across all Hartmann numbers. This behavior is linked to the greater influence of viscous forces and the reduced thermal diffusivity at higher

Prandtl numbers. As Pr increases, the momentum boundary layer thickens while the thermal boundary layer becomes thinner. This thinner thermal boundary layer intensifies the temperature gradient near the heated surface, thereby enhancing heat transfer and yielding a higher Nusselt number.

Furthermore, although the effect of Hartmann number on Nu is qualitatively similar across different Prandtl numbers, it is evident that the sensitivity of Nu to changes in Prandtl number diminishes as Ha increases. This behavior can be explained by the growing influence of the Lorentz force at higher Hartmann numbers, which suppresses convective motion and thus reduces the role of boundary layer dynamics. As the magnetic field strengthens, convective heat transfer is increasingly dampened, and the system gradually transitions toward conduction-dominated heat transfer. In this conductiondominated regime, the average Nusselt number along the inner cylinder tends to approach the asymptotic value predicted by the purely conductive solution, given by: Nu-cond= $ln(r_o-r_i)/r_iln(r_o/r_i)$  (Afrand, 2017) For instance, when R=0.9, the theoretical conductive Nusselt number is approximately Nu-cond=4.04, as determined from the equation above. This asymptotic behavior is clearly evident in Fig. 5b, where the Nusselt number approaches the conduction limit at high Hartmann numbers. In the case of R=0.9, pure conduction is practically achieved at >300, indicating that a stronger magnetic field is required to suppress convection entirely in thick annuli. Among these, potassium (Pr=0.072) demonstrated the most vigorous convective behavior, justifying its selection as the working fluid. Hence, all simulations were conducted using Ra= $10^5$  and Pr=0.072.

Figure 6 illustrates the variation of the local Nusselt number along the inner wall of an annular domain for three different aspect ratios: A=0.5, A=1, and A=2, at a fixed radii ratio R=0.9, under two magnetic field conditions: Ha=0 (no magnetic field) and Ha=40 (moderate magnetic field). In the absence of a magnetic field (Ha=0), the local Nusselt number distribution is stratified, indicating the presence of strong convective activity driven purely by buoyancy forces. This stratification becomes more pronounced for intermediate aspect ratios (particularly A=1), where the natural convection patterns are well-developed. When the magnetic field is applied (Ha=40), the stratified pattern is significantly suppressed, and the local Nusselt number distribution becomes not-uniform along the angular direction. This smoothing effect is a direct result of the Lorentz force, which dampens the velocity fluctuations and inhibits the development of convective cells, leading to a transition toward more conduction-dominated heat transfer. Moreover, the aspect ratio influences the intensity and distribution of heat transfer. For lower aspect ratios (A=0), the flow is more confined vertically, resulting in lower overall Nu values. For larger aspect ratios (A=2), the vertical space allows for the formation of stronger convective rolls under Ha=40, but these are also strongly suppressed under H=40, demonstrating the destabilizing effect of the magnetic field across all geometries.

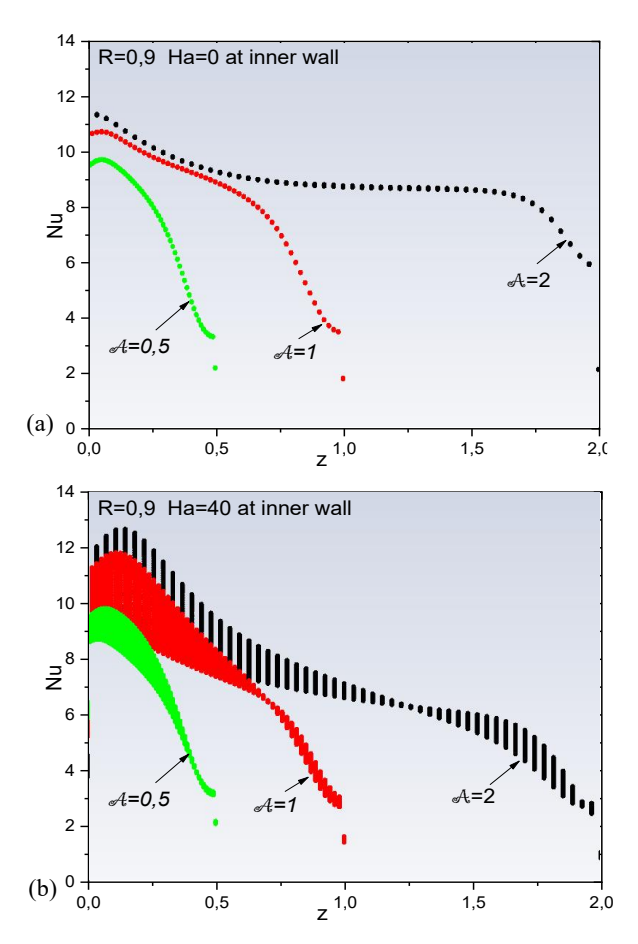


Fig. 6 Nusselt number on inner wall for three aspect ratio A = 0.5, 1,2 for(a) Ha = 0 and (b) Ha = 40

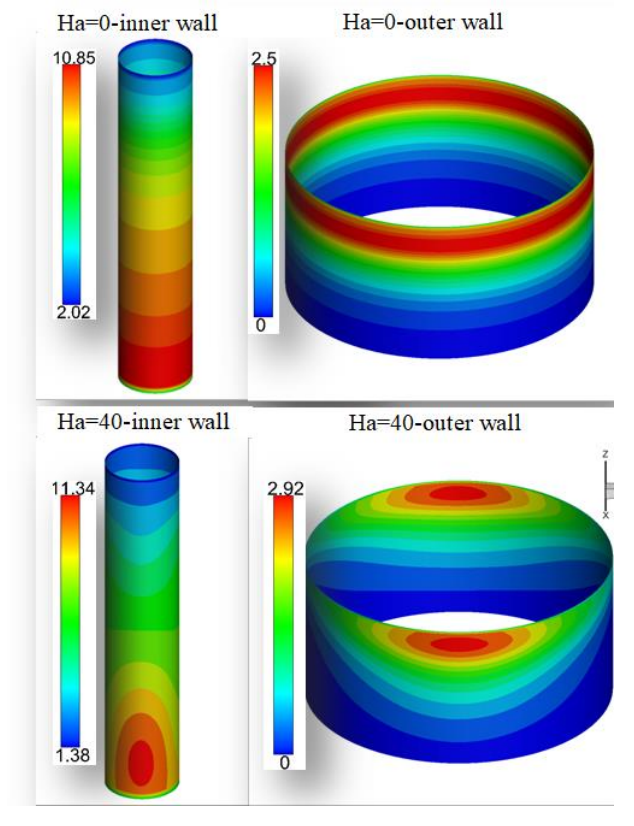


Fig. 7 3D plot of the Nusselt number on inner wall and outer wall for under Ha = 0 and Ha = 40

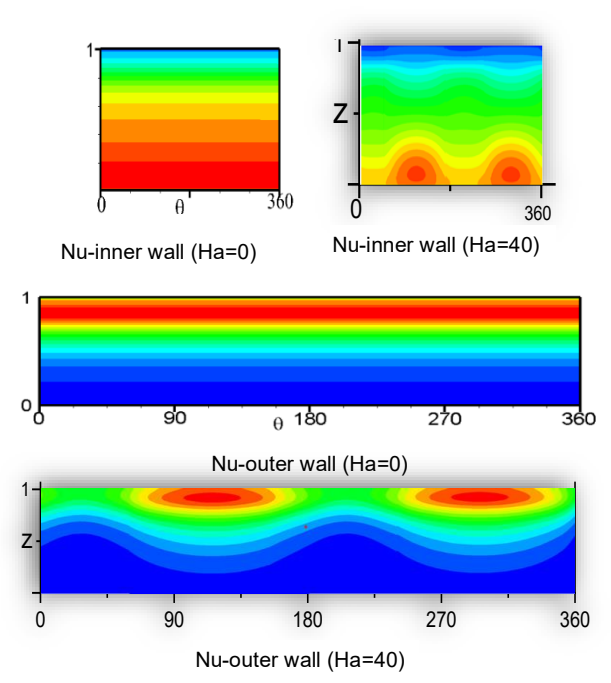


Fig. 8 Polar plot of Nusselt number distribution along the inner wall for Ha=0 and Ha=40

Figure 7 presents a three-dimensional plot of the local Nusselt number on both the inner and outer walls of the annular cavity for A = 1 and R = 0.9, under two magnetic field conditions (Ha = 0 and Ha = 40). When Ha = 0, the spatial distribution of the Nusselt number is smoother and more symmetric. The inner wall generally exhibits higher heat transfer intensity than the outer wall, which is consistent with the imposed thermal boundary conditions. In contrast, when Ha = 40, the heat transfer distribution becomes more heterogeneous on both walls, with localized peaks corresponding to regions where convective cells interact with the boundaries. This behavior highlights the suppressive effect of the magnetic field on convective motion. This trend is further confirmed by Fig. 8, which shows a polar plot of the local Nusselt number distribution along the inner wall for A = 1 and R = 0.9 under Ha = 0 and Ha = 40. Overall, the results clearly demonstrate that the application of a magnetic field leads to less uniform, more conductionlike heat transfer, and that the inner and outer walls respond differently due to their distinct roles in the development of thermal boundary layers.

Figure 9 illustrates the dependence of the average Nusselt number on the annular gap ratio (R), aspect ratio (A), and Hartmann number (Ha). Subfigures (a), (b), and (c) present two-dimensional trends: (a) average Nusselt number (Av-Nu) versus R at A=1; (b) Av-Nu versus A for a fixed R=0.9; and (c) Av-Nu versus A at two values of R=0.7and R=0.9 all evaluated under increasing Hartmann numbers. Subfigure (d) provides a three-dimensional representation that captures the combined influence of R, A, and Ha on convective heat transfer. From Fig.9(a) and 9(c), it is observed that the average Nusselt number increases with the annular gap ratio R, while it decreases with increasing Ha. In Fig. 9(b), two distinct regimes are identified: for A<1, increasing the annulus height enhances convective flow, leading to

higher Nusselt numbers, in agreement with findings reported in (Kuehn & Goldstein, 1976), conversely, for A>1, the Nusselt number decreases as heat transfer becomes concentrated near the base of the heated wall,

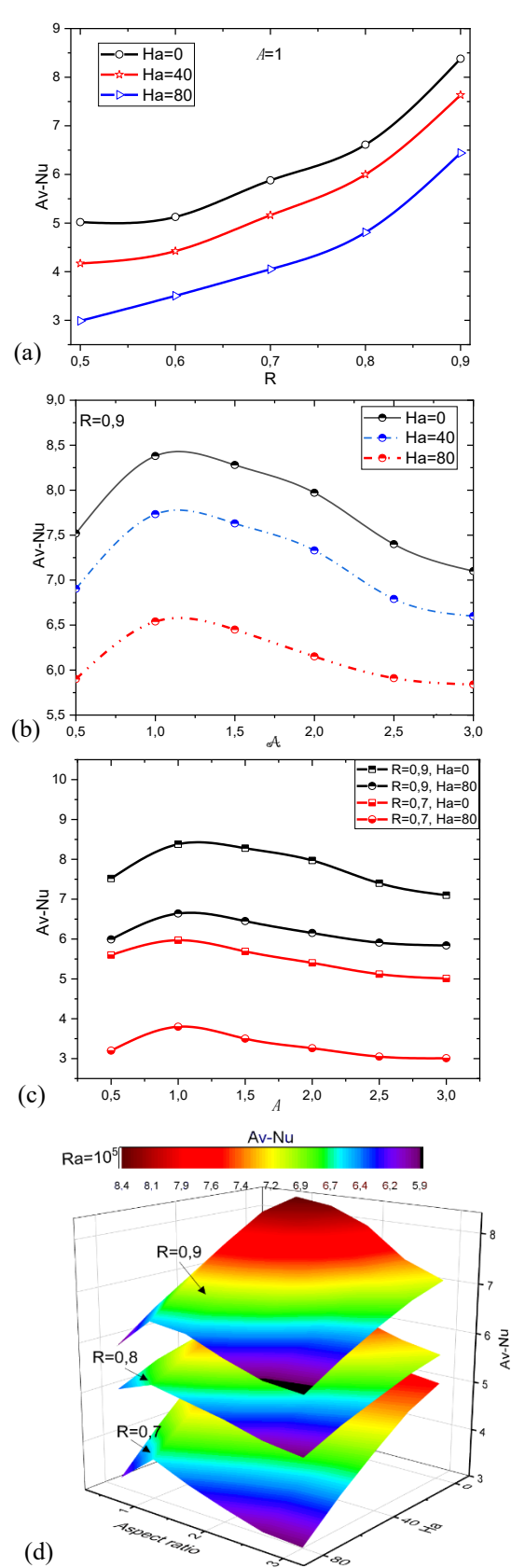


Fig. 9 (a) Av-Nu vs. R (A=1), (b) Av-Nu vs. A (R=0.9), (c) Av-Nu vs. A (R=0.7and 0.9) for Ha=0 and Ha=80. (d) 3D Av-Nu vs. Ha and R (A=1)

consistent with observations by Afrand et al. (2017). The 3D plots in Fig. 9(d) further demonstrate that increasing R enhances heat transfer across all Hartmann numbers, primarily due to curvature-induced increases in fluid velocity and the formation of thinner thermal boundary layers (Prasad & Kulacki, 1984). At higher Hartmann numbers, the Lorentz force strongly suppresses flow instabilities and turbulent fluctuations, resulting in reduced velocity gradients and a shift toward conduction-dominated heat transfer, as evidenced by the lower Nusselt numbers. These findings emphasize the intricate interplay between the geometric parameters (R, A) and the magnetic field strength (Ha) in controlling convective heat transfer within annular domains.

## 4.2 Analysis of Temperature, Lorentz Force, Induced Fields

The flow within an annular gap can be categorized into three distinct regions: the core region, the Hartmann layer, and the Roberts layer. The minimum theoretical thicknesses of the Hartmann and Roberts layers are proportional to Ha<sup>-1</sup> and Ha<sup>-1/2</sup>, respectively. Within the Hartmann layer adjacent to walls normal to the applied magnetic field, viscous forces compete with magnetic forces. Since all walls are electrically insulating, electric currents remain confined within the fluid, generating a Lorentz force. As the Lorentz force intensifies, the buoyancy-driven layer initially governed by a balance between buoyancy and viscous forces is progressively supplanted by the Hartmann layer, electromagnetic and viscous forces equilibrate (Mahfoud, 2023). Under a radial magnetic field, the Lorentz force fluid suppresses accelerates the and flow inhomogeneities, eliminating convection once the field strength exceeds a critical threshold.

Figure 10 demonstrates the influence of a magnetic field on temperature distributions, visualised on the vertical median (x-y) plane and the isosurface  $\Theta =$ 0.8, and azimuthal velocity profiles at vertical positions z = 0.1 and z = 0.9, for parameters R = 0.9 and A = 1. In the absence of a magnetic field (Ha = 0), isotherms exhibit axisymmetric behaviour. However, at a Hartmann number of 40, distinct thermal stratification emerges in the y-plane, whilst the x-plane remains unaffected. This asymmetry stems from the amplified Lorentz force in the y-plane, which suppresses fluid motion and disrupts convective heat transfer. A striking enhancement in tangential velocity occurs at the cylinder's base, where w = 13.2 for Ha = 80, compared with w = 0.03 for Ha = 0. These magnetic layers fundamentally alter velocity and thermal profiles, marking a shift from buoyancydominated convection to MHD-governed dynamics.

Figure 11 illustrates the influence of the magnetic field on isotherms, Lorentz force, and induced electric fields in vertical (x-y plane) and horizontal (z-plane) cross-sections for an annular gap configuration (R=0.9, A=1) under a strong magnetic field (Ha=80). The left panel highlights the thermal patterns, showing a transition of the isotherms from axisymmetric distributions at Ha=0 (as seen in Fig. 10) to asymmetric stratification in the y-plane at Ha=80. This anisotropy results from the Lorentz force suppressing convective

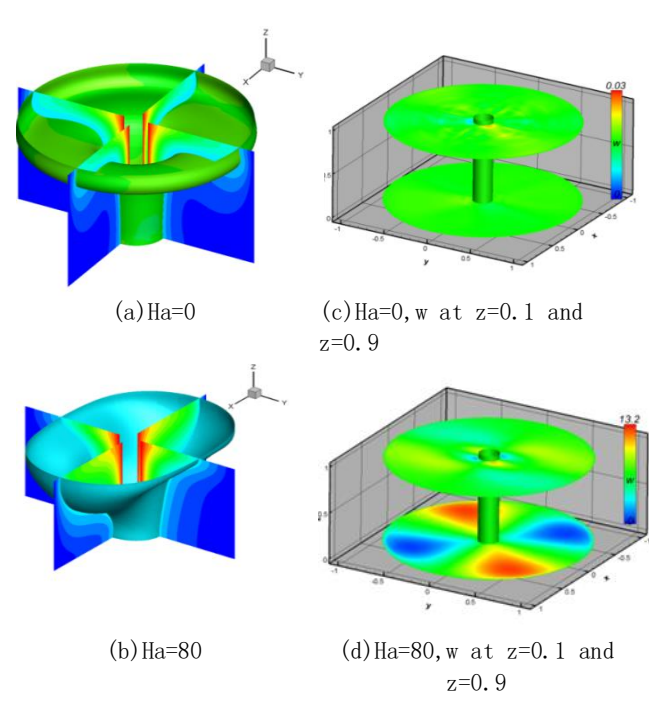


Fig. 10 Magnetic field effects on (a-b) temperature plotted on the vertical median (x-y) plane, and isosurface  $\Theta$ =0.8; (c-d) azimuthal velocity contours

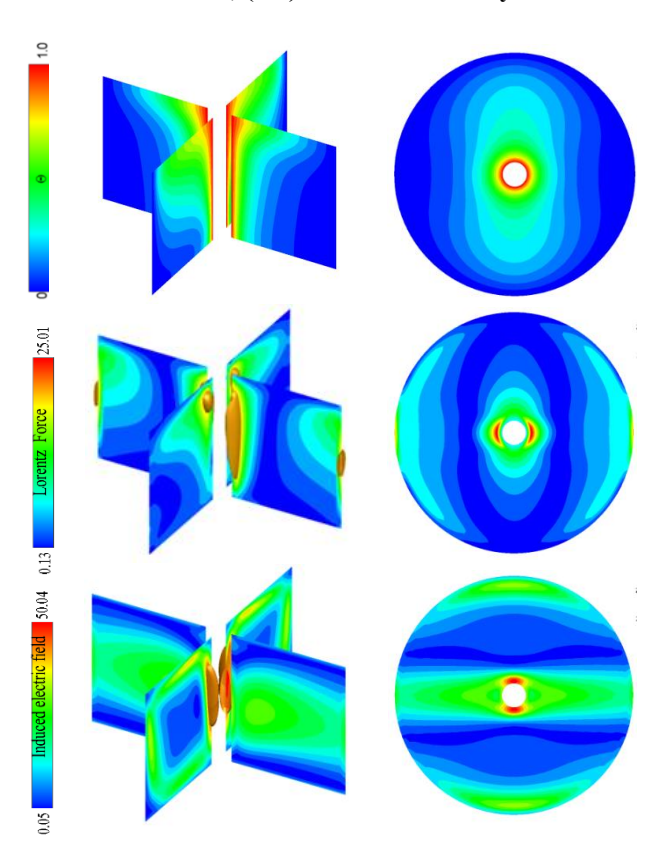


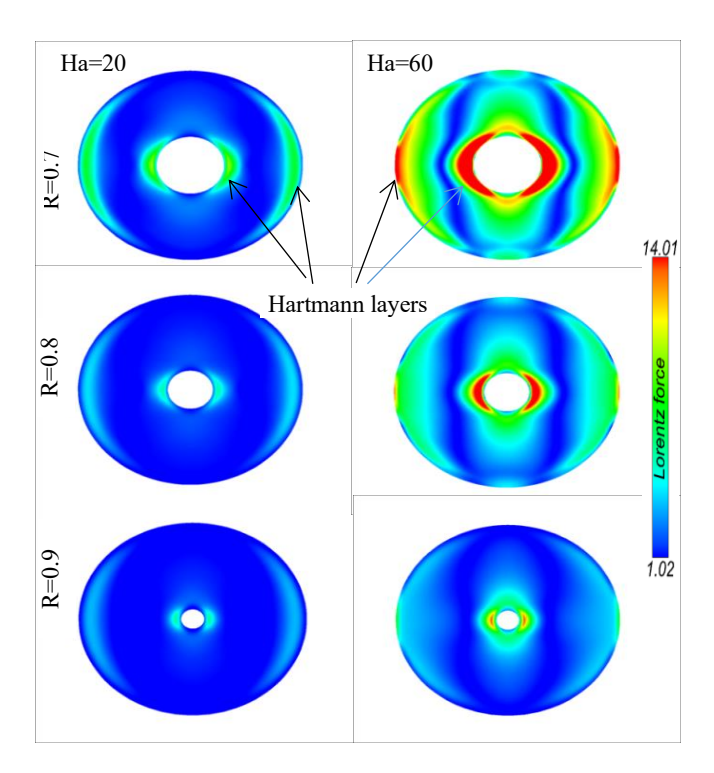
Fig. 11 Magnetic effect on isotherms, Lorentz force and induced electric field in the (left) vertical median planes and (right) horizontal median plane

motion in the y-plane, whilst the x-plane remains largely unaffected thermally. The Lorentz force distribution (center panel) confirms its dominance in the y-plane, where it peaks at  $F_{max}\approx 25$ , contrasting with weaker effects in the x-plane. Conversely, the x-plane exhibits significant induced electric potential ( $E_{max}\approx 50$ ), a result

of the magnetic field's y-axis alignment. The horizontal median plane (bottom panel) reveals vertical electric field contours, with maxima localised in the x-plane and minima in the y-plane. This asymmetry arises from the orientation of **B**: In the y-plane, it is perpendicular to the vorticity vector ( $\nabla \times \mathbf{U}$ ), which suppresses the induced electric potential as described by Eq. (4). In contrast, the x-plane alignment permits significant U × B motional induction, resulting in pronounced electric potential peaks. Equation 5 clarifies the competition between induced (E') and motional  $(U \times B)$  currents. In regions where these components cancel each other, the net current density becomes negligible ( $j \approx 0$ ). Elsewhere, the dominance of one term over the other determines the Lorentz force direction, which always opposes the main flow. These trends, consistent across annular gaps, underscore the magnetic field's role in reshaping thermal and momentum transport. The suppression of convection in the y-plane and enhanced electric effects in the x-plane highlight the transition from buoyancy-driven to MHD dominance at high Ha.

Figure 12 presents a comparative analysis of the Lorentz force and induced electric field distributions in the horizontal midplane (z = 0.5) for various annular gap ratios (R = 0.7, 0.8, 0.9) and Hartmann numbers (Ha = 20and 60). The results reveal the presence of two distinct electromagnetic boundary layers. Hartmann layers, located adjacent to walls perpendicular to the magnetic field, exhibit strong Lorentz forces due to the direct interaction between the magnetic field and flow vorticity  $(\nabla \times \mathbf{U})$ . When R = 0.7 and Ha = 60, the Lorentz force reaches a maximum of approximately  $F_{max} \approx 14$ . In contrast, Roberts's layers are characterised by dominant induced electric fields, peaking at  $E_{max} \approx 42$  for the same parameters. These layers arise from the alignment of the vorticity vector with the magnetic field, which enhances motional induction  $(\mathbf{U} \times \mathbf{B})$  and leads to steep velocity gradients.

The radial orientation of the magnetic field introduces anisotropy in the flow. In the y-plane, Lorentz forces suppress the flow, demonstrating strong electromagnetic damping. Conversely, in the x-plane, the radial alignment of velocity vectors minimises  $\mathbf{U} \times \mathbf{B}$ , resulting in negligible Lorentz forces but significant enhancement of the induced electric fields. Increasing the Hartmann number intensifies both electromagnetic components, sharpening the boundary layer contrasts. For example, doubling Ha from 20 to 60 increases  $F_{max}$  by approximately 50% for R = 0.7. Meanwhile, increasing the annular gap ratio R promotes higher fluid velocities due to reduced geometric confinement, which enhances Lorentz forces (e.g.  $F_{max} \approx 14.01$  at R = 0.7) but paradoxically diminishes local electric fields. This reduction is attributed to partial cancellation of the induced electric field E' by the motional term  $U \times B$ . Despite localised reductions, the overall electric field magnitude tends to increase with R. Furthermore, the emergence of regions where  $\mathbf{j} \approx 0$  demonstrates MHD's intrinsic capability to balance induced and motional effects, a critical mechanism for stabilising turbulent or unstable flows.



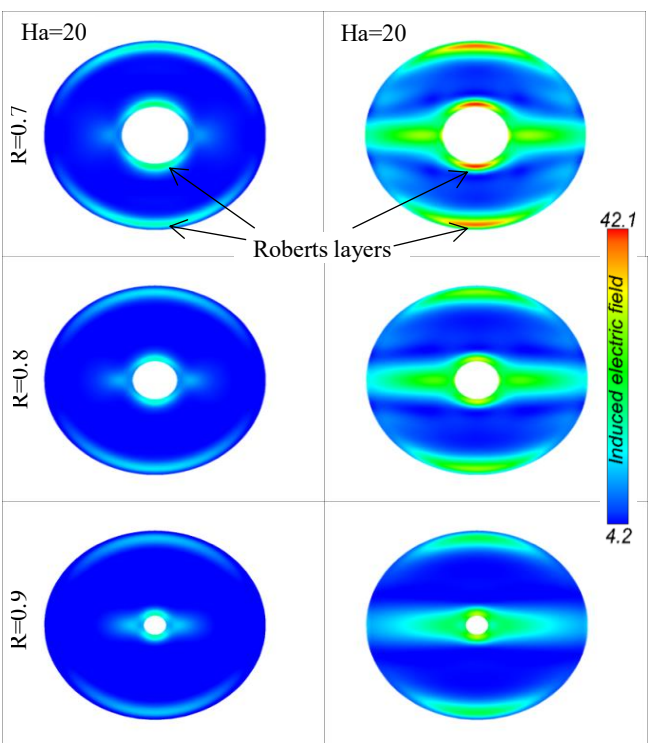


Fig. 12 Contour plots of Lorentz force and induced electric field in the horizontal mi-plane (z = 0.5) for Ha = 20 (left) and Ha = 60 (right), with A = 1

Figure 13 explores the interplay between electrically conductive walls and magnetic effects on heat transfer, quantified through local and average Nusselt numbers along the inner wall for an annular gap R=0.9 and A=1. For Ha = 0, natural convection dominates, yielding a peak local Nu of 10.85 and an Av-Nu of 8.38. For Ha =60, insulating walls (EI) exhibit heightened localised heat transfer (Nu<sub>max</sub> = 11.34) but reduced bulk convection (Av-Nu = 6.96), reflecting Lorentz-force suppression. EC-V further diminishes both metrics (local

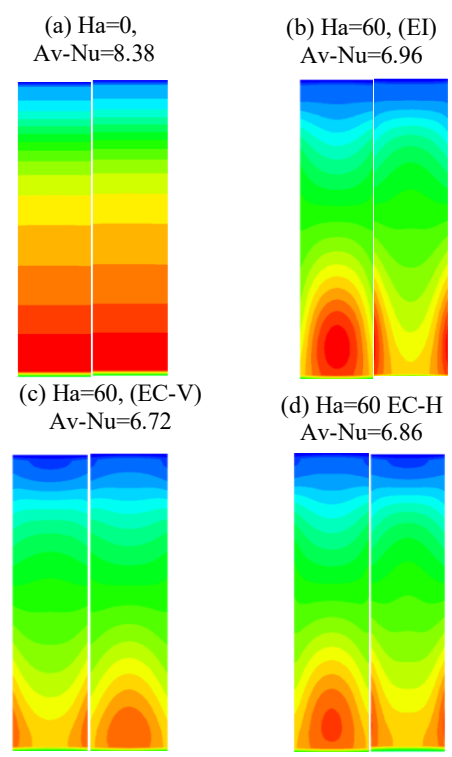


Fig. 13 Local Nusselt for Ha = 0 and Ha = 60

 $Nu_{max} = 10.44$ , Av-Nu = 6.72) due to radial current leakage amplifying electromagnetic dissipation, whilst EC-H partially mitigates damping (Av-Nu = 6.86, local  $Nu_{max} = 10.65$ ) by preserving inertial effects. This asymmetry underscores that vertical conductive walls intensify Lorentz losses, whereas horizontal ones stabilise local flow.

Figure 14 shows that for Ha = 80 and R = 0.7, the EC-H configurations outperform both EI and EC-V at lower heights (z < 0.2) due to the dominance of inertial effects in wider gaps. Across R = 0.5–0.87, EC-H enhances heat transfer by eliminating Hartmann layers and sustaining inertial flow, but beyond R > 0.87, geometric constraints dominate, favouring EI configurations which restrict current leakage. A critical transition at R  $\approx$  0.87 suggests that EC-H optimises thermal performance in moderate gaps, whilst EI is more effective in narrow geometries. Conductive walls reshape current pathways, weakening viscous boundary layers but introducing trade-offs: (EC-V) consistently underperforms due to disrupted circulation, while (EC-H) optimizes heat transfer in by harmonizing inertial and electromagnetic effects.

# 4.3. Effects of Electrically Conductive Boundaries on Induced Fields and Lorentz Forces

Figures 15–16 explore the influence of wall electrical conductivity on the distributions of induced electric fields and Lorentz forces within a vertical cylindrical annulus subjected to a radial magnetic field (Ha = 80). The configuration with electrically insulated walls (EI) shows strong confinement of current within the fluid, resulting in a maximum induced electric field of 75.1 in the x-plane and a reduced value of 50.82 in the y-plane due to asymmetric current circulation. When the top and

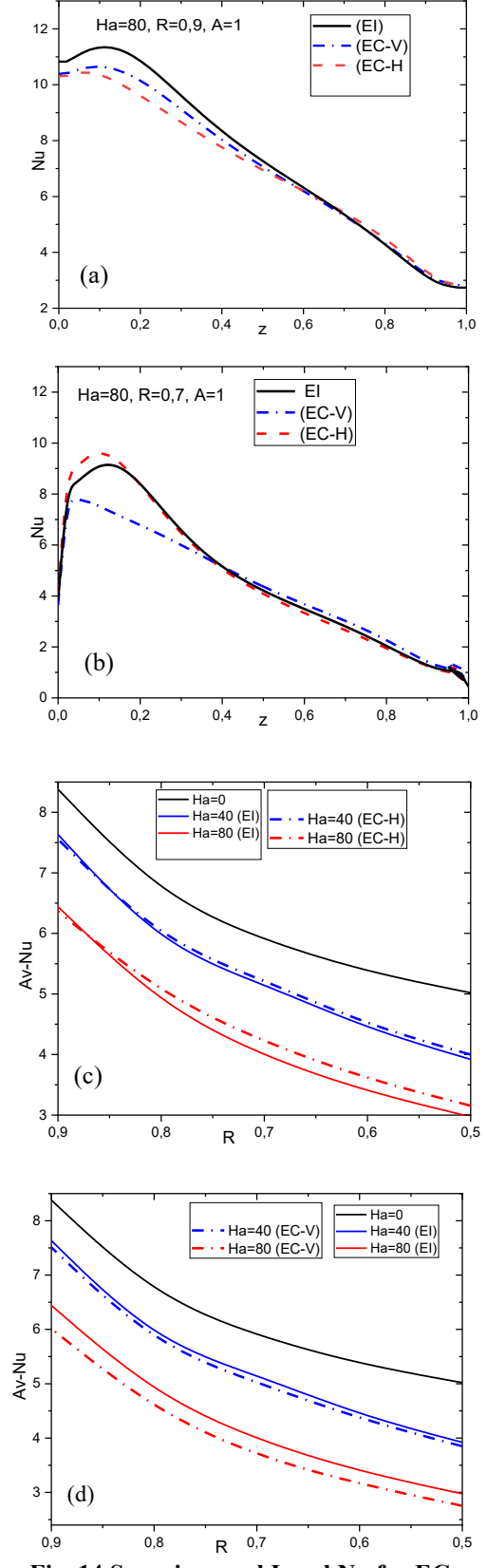


Fig. 14 Superimposed Local Nu for EC-wall configurations at A = 1 with (a) Ha = 80, R = 0.9 and (b) Ha = 80, R = 0.7. Average Nu vs. R for A = 1 with (c) EC-H and EI-walls (d) EC-V and EI-walls

bottom walls are made conductive (EC-H), slight current leakage reduces the x-plane field to 73.1, while it maintains moderate strength in the y-plane. In contrast,

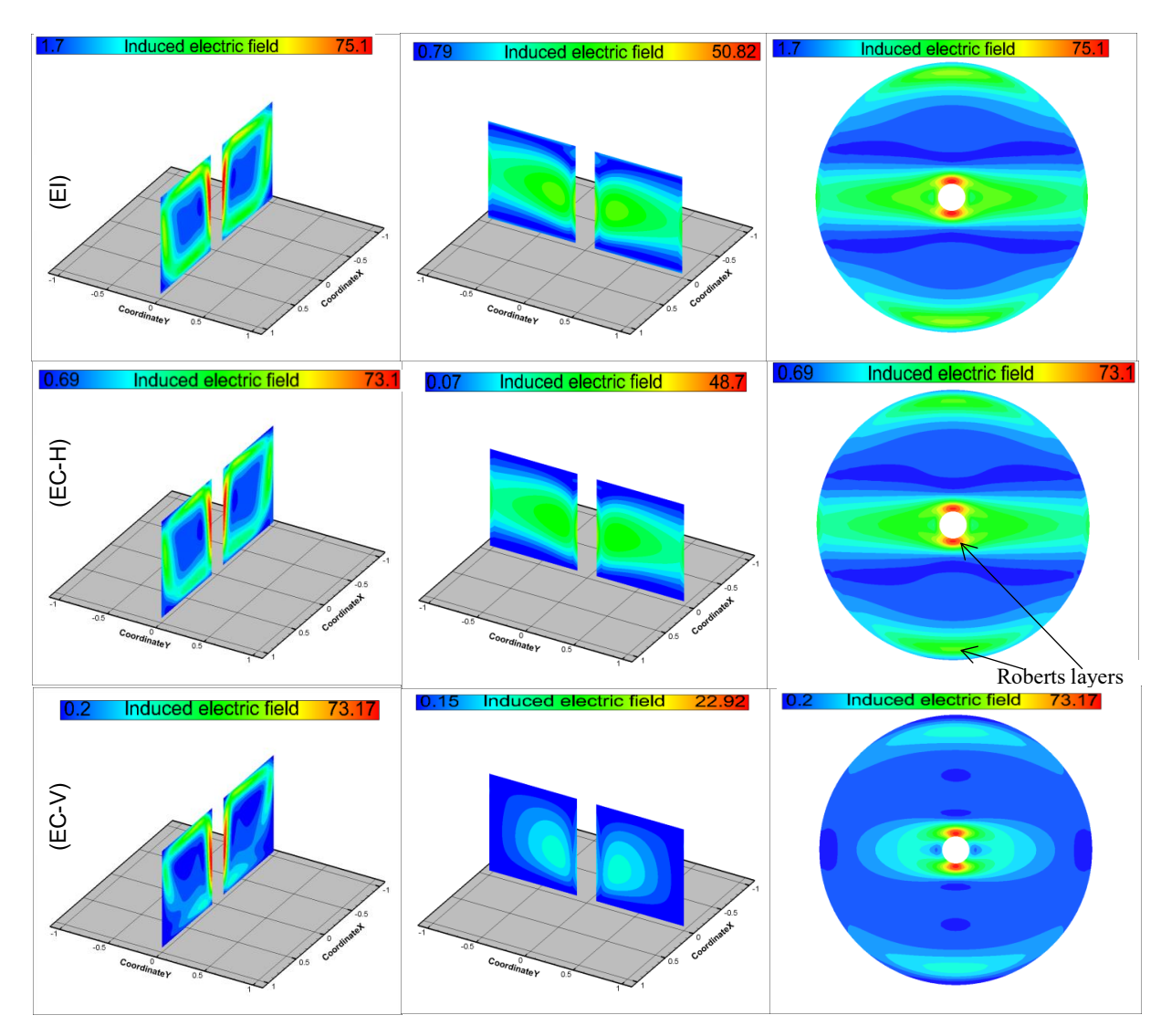


Fig. 15 Induced electric field contours (median/horizontal planes) when Ha=80

the configuration with conductive vertical walls (EC-V) significantly alters the current pathways: short-circuiting through the radial boundaries drastically reduces the y-plane field to 22.92, demonstrating the dominant role of vertical conductivity in dissipating current.

The Lorentz force distribution exhibits strong directional asymmetry, with consistently higher magnitudes in the y-plane due to the effective coupling between the radial magnetic field and azimuthal currents. In the EI case, the peak Lorentz force reaches 20.18 in the y-plane versus 17.72 in the x-plane. The EC-V configuration, despite its lower bulk electric field, yields the highest localized Lorentz force (20.71) near the conductive walls in the y-plane, while the x-plane force drops to 16.55 due to the suppression of transverse currents. The EC-H configuration produces intermediate force levels (e.g., 16.55 in the x-plane), reflecting partial current diversion through horizontal walls.

Consequently, conductive walls act as current sinks, reducing the overall electric field within the fluid but intensifying localized Lorentz forces near the boundaries. At high Hartmann number (Ha = 80), this behavior results in the formation of thin Hartmann layers along

conductive surfaces, where the balance between viscous and electromagnetic forces becomes dominant. The annular geometry further accentuates directional effects by allowing optimal coupling of the radial magnetic field with azimuthal currents in the y-plane, explaining the consistently stronger forces observed in this direction.

Contour plots in the horizontal mid-plane (z=0.5) further reveal spatial reorganization under different conductivity scenarios. The EC-V configuration disrupts the classical Roberts layer typically present near the outer wall, highlighting how vertical wall conductivity modifies canonical MHD flow structures. While EI and EC-H configurations show nearly axisymmetric force distributions, EC-V produces highly asymmetric, localized forces concentrated near the conductive vertical boundaries, which aligns with the observed peak of 20.71 in the y-plane.

### 5. CONCLUSION

A three-dimensional numerical investigation was performed to examine natural convection of liquid metal in a vertical cylindrical annulus exposed to a radial

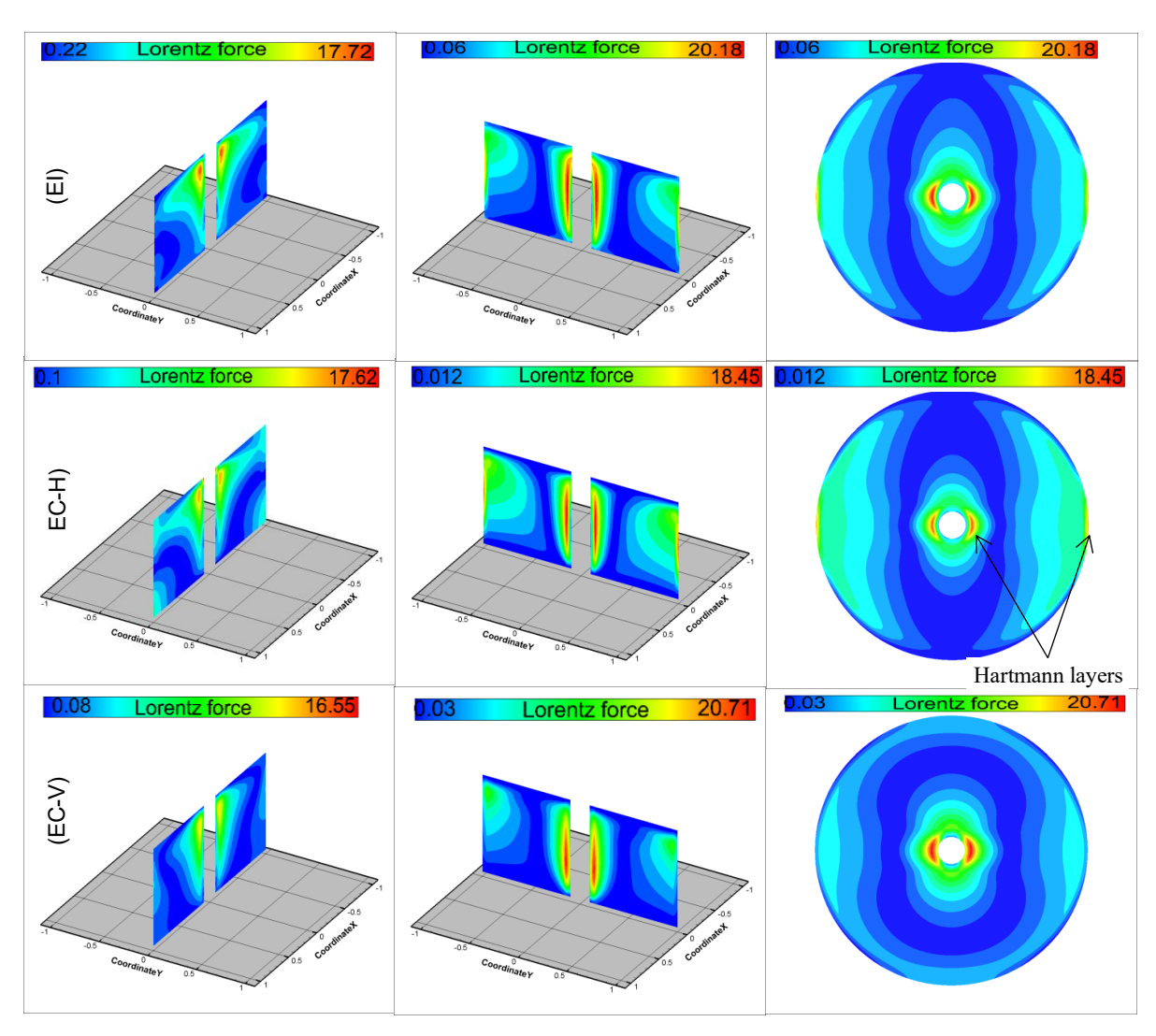


Fig.16. Lorentz force contours (median/horizontal planes) when R=0.9, Ha=80 and A=1.

magnetic field. The focus was on understanding how wall electrical conductivity, Lorentz forces, and geometric factors affect flow dynamics and heat transfer behavior. Key findings include:

- Increasing the Rayleigh number from Ra=10<sup>4</sup> to Ra =10<sup>5</sup> significantly strengthens convective currents. The higher Rayleigh number provides a more realistic representation of the coupled thermal and fluid dynamics in the system.
- (EC-H) yields the highest average Nusselt number (6.86 at R = 0.9, Ha = 60), with an increase of 1.4% compared to EI and 2.1% compared to (EC-V). Gains reach up to approximately 10% for R < 0.87, while EI outperforms (EC-H) for R > 0.87. (EC-V) consistently exhibits lower performance, with reductions of 3–5% compared to (EI).
- Increasing the Hartmann number (Ha) enhances the Lorentz force, which suppresses convective motion. At high-Ha, the heat transfer becomes nearly conduction-dominated, especially in thick annuli.
- For A<1, heat transfer improves due to enhanced convection. For A>1, thermal stratification suppresses

convection, leading to a monotonic decrease in Nusselt number. Increasing the annular gap R enhances heat transfer by allowing more fluid motion and space for convection.

- The magnetic field generates Hartmann layers on walls perpendicular to its direction and Roberts's layers on parallel walls. These boundary layers disrupt the symmetry of the natural convection flow.
- The EC-V configuration is most effective for intermediate radius ratios (R≈0.5–0.87) under strong magnetic fields, as it reduces Lorentz damping and supports fluid momentum.
  - (EI) case is more effective at larger gaps (R>0.87), limiting current leakage and maintaining strong electromagnetic interactions in the fluid bulk.
  - It is recommended that future studies investigate the influence of wall thickness on induced current distributions, particularly in systems with conductive boundaries.

#### **ACKNOWLEDGEMENTS**

The authors gratefully acknowledge the support of the General Directorate of Scientific Research and Technological Development (Algeria).

#### **CONFLICT OF INTEREST**

The author declares that there is no conflict of interest regarding the publication of this article.

#### **AUTHORS CONTRIBUTION**

**Brahim Mahfoud:** Visualization, and supervision, numerical simulations, revision of the manuscript. **Lakhdar Bouagbi**: Numerical simulations, validation. **Hibet Errahmane Mahfoud**: Writing, review & editing. All authors have read and agreed to the published version of the manuscript.

#### REFERENCES

- Abou-Sena, A., Arbeiter, F., & Böttcher, T. (2016). Study of the wettability of fusion relevant steels by the sodium potassium eutectic alloy NaK-78, *Nuclear Materials and Energy*, *9*, 292–299. https://doi.org/10.1016/j.nme.2016.05.003.
- Afrand, M. (2017). Using a magnetic field to reduce natural convection in a vertical cylindrical annulus. *International Journal of Thermal Sciences*, 118,12-23. https://doi.org/10.1016/j.ijthermalsci.2017.04.012
- Ali, K., Ahmad, S., Ahmad, S., & Tayebi, T. (2023). Impact of magnetic field localization on the vortex generation in hybrid nanofluid flow. *Journal of Thermal Analysis and Calorimetry*, 148(13), 6283–6300. https://doi.org/10.1007/s10973-023-12104-5
- Benhacine, H., Mahfoud, B., & Salmi, M. (2022a). Stability effect of an axial magnetic field on fluid flow bifurcation between coaxial cylinders. International Journal of Computational Materials Science and Engineering, 10(4), 2150023. https://doi.org/10.1142/S20476841215002 38
- Benhacine, H., Mahfoud, B., & Salmi, M. (2022b). Stability of an Electrically Conducting Fluid Flow between Coaxial Cylinders under Magnetic field. *Journal of Applied Fluid Mechanics*, 15(2), 1741-
  - 1753. https://doi.org/10.47176/JAFM.15.02.33050
- Ben Salah, N., Soulaimani, A., & Habashi, W. G. (2001). A finite element method for magnetohydrodynamics. Computer Methods in Applied Mechanics and Engineering, 190(43), 5867–5892. https://doi.org/10.1016/S0045-7825(01)00256-3
- Boccaccini, L. V. (2013). Progress in EU blanket technology, Fusion Science and Technology, 64(3),

- pp. 615–622. <a href="https://doi.org/10.13182/FST13-419160">https://doi.org/10.13182/FST13-419160</a>.
- Boyd, J. P. (2000). *Chebyshev and Fourier Spectral Methods* (2nd ed.). Dover Publications. ISBN: 0486411834.
- Dash, S. C., & Singh, N. (2019). Effect of a strong axial magnetic field on swirling flow in a cylindrical cavity with a top rotating lid. *International Journal of Modern Physics C*, 30(11), 1950092. <a href="https://doi.org/10.1142/S01291831195009">https://doi.org/10.1142/S01291831195009</a>
- Jha, B. K., & Aina, B. (2018). Impact of viscous dissipation on fully developed natural convection flow in a vertical microchannel. *Journal of Heat Transfer*, 140(9), 094502. https://doi.org/10.1115/1.4039641
- Kakarantzas, S. C., Sarris, I. E., & Vlachos, N. S. (2014). Magnetohydrodynamic natural convection liquid metal between coaxial isothermal cylinders due to internal heating. Numerical Heat Transfer, Part 65. 401-418. Ahttps://doi.org/10.1080/10407782.2013.831681
- Kuehn, T. H., & Goldstein, R. J. (1976). An experimental and theoretical study of natural convection in the annulus between horizontal concentric cylinders. *Journal of Fluid Mechanics*, 74(4), 695–719. https://doi.org/10.1017/S0022112076002012
- Kumar, A., & Singh, A. K. (2013). Effect of induced magnetic field on natural convection in vertical concentric annuli heated/cooled asymmetrically. *Journal of Applied Fluid Mechanics*, 6(1),15-26.https://doi.org/10.36884/jafm.6.01.19477
- Leela, V., Prasannakumara, B. C., Shilpa, B., & Gangadhara Reddy, R. (2022). Computational analysis of ohmic and viscous dissipation effects on MHD mixed convection flow in a vertical channel with linearly varying wall temperatures. Proceedings of the Institution of Mechanical Engineers, Part E: Journal of Process Mechanical Engineering. Feb 24, 2022. https://doi.org/10.1177/09544089221080669
- Leonchuk, S. S., Falchevskaya, A. S., Nikolaev, V., Vinogradov, V. V. (2022). NaK alloy: underrated liquid metal, *Journal of Materials Chemistry A*, 10(43), 22955–22976. https://doi.org/10.1039/D2TA06882F.
- Mahfoud, B. (2022), Simulation of magnetic field effect on heat transfer enhancement of swirling nanofluid,"

  International Journal of Computational Materials Science and Engineering. 11(04), 2250007. https://doi.org/10.1142/S204768412250007
- Mahfoud, B. (2023). Enhancement heat transfer of swirling nanofluid using an electrical conducting lid. *Journal of Thermophysics and Heat Transfer*, 37(1), 263–271. https://doi.org/10.2514/1.T6550
- Mozayyeni, H. R., & Rahimi, A. B. (2012). Mixed convection in cylindrical annulus with rotating outer

- cylinder and constant magnetic field with an effect in the radial direction. *Scientia Iranica*, *19*(1), 91–105. <a href="https://doi.org/10.1016/j.scient.2011.12.006">https://doi.org/10.1016/j.scient.2011.12.006</a>
- Ni, M. J., Yang, J. C., & Zhang, D. J., (2025). Magnetohydrodynamics in liquid metal interfacial flows, *Applied Mechanics Reviews*, 1–105. https://doi.org/10.1115/1.4067935.
- Prasad, V., & Kulacki, F. A. (1984). Natural convection in a vertical porous annulus. *International Journal of Heat and Mass Transfer*, 27(2), 207–219. https://doi.org/10.1016/0017-9310(84)90212-6
- Roux, N., Johnson, C., & Noda, K. (1992). Properties and performance of tritium breeding ceramics, *Journal of Nuclear Materials*, *191*, 15–22. https://doi.org/10.1016/S0022-3115(09)80005-6.
- Sankar, M., Venkatachalappa, M., & Do, Y. (2011). Effect of magnetic field on the buoyancy and thermocapillary driven convection of an electrically conducting fluid in an annular enclosure. *International Journal of Heat and Fluid Flow*, 32, 402–412. <a href="https://doi.org/10.1016/j.ijheatfluidflow.2010.12.001">https://doi.org/10.1016/j.ijheatfluidflow.2010.12.001</a>
- Sankar, M., Venkatachalappa, M., & Shivakumara, I. S. (2006). Effect of magnetic field on natural convection in a vertical cylindrical annulus. *International Journal of Engineering Science*, 44, 1556-1570. https://doi.org/10.1016/j.ijengsci.2006.06.004
- Selim, M. M., El-Safty, S., Tounsi, A., & Shenashen, M. (2023). Review of the impact of the external magnetic field on the characteristics of magnetic nanofluids. *Alexandria Engineering Journal*, 76, 75–89. https://doi.org/10.1016/j.aej.2023.06.018
- Shilpa, B., Leela, V., & Rani, H. P. (2023). Stability analysis of MHD radiative mixed convective flow in vertical cylindrical annulus: thermal nonequilibrium approach. *Heat Transfer*, 52(1), 707-733. https://doi.org/10.1002/htj.22713
- Shoaib, M., Tabassum, R., Nisar, K. S., Raja, M. A. Z., Rafiq, A., Khan, M. I., Jamshed, W., Abdel-Aty, A.-

- H., Yahia, I. S., & E. Mahmoud, E. (2021). Entropy optimized second grade fluid with MHD and Marangoni convection impacts: an intelligent neurocomputing paradigm. *Coatings*, *11*, 1492. <a href="https://doi.org/10.3390/coatings11121492">https://doi.org/10.3390/coatings11121492</a>
- Teimouri, H., Afrand, M., Sina, N., Karimipour, A., & Isfahani, A. H. M. (2015). Natural convection of liquid metal in a horizontal cylindrical annulus under radial magnetic field. *International Journal of Applied Electromagnetics and Mechanics*, 49(4), 453–461. <a href="https://doi.org/10.3233/JAE-1500">https://doi.org/10.3233/JAE-1500</a>
- Ulyanov, V. V., Koshelev, M. M., Kremleva, V. S., Bragin, D. S., & Prikazchikova, A. A. (2024). Features of purification and control of sodium-potassium eutectic alloy, *Izvestiya Vysshikh Uchebnykh Zavedenij. Yadernaya Ehnergetika*, 2, pp. 127–137. ISSN: 0204-3327.
- Wang, F., Peng, L., Zhang, Q. Z., & Liu, J. (2015). Effect of horizontal temperature difference on Marangonithermocapillary convection in a shallow annular pool. *Acta Physica Sinica*, 64(14), 140202. https://doi.org/10.7498/aps.64.140202
- Wang, X., Lu, C., & Rao, W. (2021). Liquid metal-based thermal interface materials with a high thermal conductivity for electronic cooling and bioheat-transfer applications, *Applied Thermal Engineering*, 192, 116937. <a href="https://doi.org/10.1016/j.applthermaleng.2021.11693">https://doi.org/10.1016/j.applthermaleng.2021.11693</a>
- Wrobel, W., Fornalik-Wajs, E., & Szmyd, J. S. (2010). Experimental and numerical analysis of thermomagnetic convection in a vertical annular enclosure. *International Journal of Heat and Fluid Flow*, 31(6), 1019–1031. <a href="https://doi.org/10.1016/j.ijheatfluidflow.2010.05.012">https://doi.org/10.1016/j.ijheatfluidflow.2010.05.012</a>
- Yan, Y. (2024). Experimental and numerical study of mixed-convection magnetohydrodynamic (MHD) flows for liquid-metal fusion blankets, PhD Dissertation, University of California, Los Angeles.